Supporting Information

Dönhöfer et al

SI Text

Interaction of TetM with the ribosome. The major sites of contact involve domains III and IV of TetM with the small subunit and domains I and V of TetM with the large subunit (***SI Appendix,* Fig. S7**). Like EF-G and LepA, domain III of TetM interacts with ribosomal protein S12 on the small subunit (***SI Appendix,* Fig. S7A**), however, unlike EF-G and LepA, no interaction was observed between domain II and helix 5 (h5) or h15 of the 16S rRNA (***SI Appendix,* Fig. S7B**). This is likely due to the aforementioned shift in orientation of EF-G towards the small subunit compared to TetM (***SI Appendix,* Fig. S6**). Domain IV of TetM interacts with the cleft between the head and body of the small subunit (**Fig. 3A**), with loop II between $\beta 4_4$ and αA_4 interacting with the proximal end of helix 34 of the 16S rRNA, such that residues Ser465-Leu466-Gly467 ($_{465}$SLG$_{467}$) come into close proximity with the backbone of C1209 and the nucleobase of C1214 (**Fig. 3C**). Loop III of TetM linking $\beta 5_4$ to helix αB_4 fuses directly with C1054 of the 16S rRNA, a component of the primary tetracycline binding site (**Fig. 3C**). The CTE interacts with loop I of domain IV of TetM, but also with H69 of the 23S rRNA as well as h44 of the 16S rRNA (**Fig. 2D,E** and ***SI Appendix,* Fig. S7C,D**). We believe that interaction of the CTE with h44 stabilizes the flipped-out conformation of A1492 and A1493 (seen in **Fig. 2D,E**), since this conformation not only correlates with the electron density of the fused density between h44 and the CTE (**Figure 3F**), but also explains better the hole in the density of helix 44 compared with conformation when A1492 and A1493 are stacked within h44 (***SI Appendix,* Fig. S7C,D**).

On the large subunit, the bulk of the interactions of TetM are with ribosomal proteins L6, L7 and L11 as well as helices H43/H44, H89 and H95 of the 23S rRNA (***SI Appendix,* Fig. S7E-H**). The C-terminus of L6, which contains two terminal lysine residues (K175 and K176), extends towards the distal end of αB_5 of domain V of TetM, as was reported for EF-G (1) (***SI Appendix,* Fig. S7E**). Density for the neighboring loop of TetM connecting αB_5 with $\beta 4_5$ fuses with nucleotide A2660 located at the tip of the sarcin-ricin loop (SRL, H95) (***SI Appendix,* Fig. S7E**). Cleavage, depurination or mutation at this position in the SRL leads to defects in EF-

G GTPase activity (2, 3). In the TetM●70S map, additional density is observed adjacent to L11-NTD in the position where the C-terminal domain of L7 (L7-CTD) has been previously observed to interact with EF-G (1, 4, 5) (***SI Appendix,* Fig. S7F**).

Domain V of TetM also forms a large network of interactions that encompass the stalk base and H89 (***SI Appendix,* Fig. S7G**): The proximal portion of helix αA_5 of TetM contacts nucleotide U2473 at the tip of H89 whereas the mid to distal portions of α-helix A_5 appear to fuse with the nucleotides A1067 and A1095 located at the tips of H43 and H44, respectively (***SI Appendix,* Fig. S7G**). This region encompasses the binding site of the thiopeptide antibiotics thiostrepton and micrococcin, which inhibit TetM and TetO GTPase activity (6-8).

The network of interactions of domain V of TetM with the stalk base also encompasses interaction between the distal end of β-strand 2_5 and the proline-rich 3_{10} helix within the N-terminal domain (NTD) of L11 (***SI Appendix,* Fig. S7G**). The stalk base is flexible and is found in a different position in TetM●70S compared to EF-G●70S (1, 9). Moreover, in such EF-G●70S complexes, the L11-NTD is observed in an open conformation, shifted away from H43/H44 (**Fig. 1D** and ***SI Appendix,* Fig. S6**). In contrast, in TetM●70S, the L11-NTD adopts a more closed conformation (***SI Appendix,* Fig. S7G**), with density connecting H43/44 with L11-NTD observable. This difference in the conformation of the stalk base in TetM●70S and EF-G●70S is in agreement with the distinct footprinting patterns observed in this region upon binding of TetO and EF-G to the ribosome (7). The conformation and position of the stalk base in TetM●70S is rather more similar to that observed when EF-Tu●tRNA is bound to the 70S ribosome (10, 11) (***SI Appendix,* Fig. S6**). TetO binding has been proposed to invoke a conformational change in the ribosome that persists after it has left the ribosome, explaining how TetO can enhance the ribosome-dependent GTPase activity of EF-Tu (7). A specific conformation and optimal positioning of the stalk base by TetM that enhances EF-Tu activity may thus contribute to the observed synergy between these two factors.

The sarcin-ricin loop (SRL, H95) also establishes a number of interactions with the G domain (domain I) of TetM (***SI Appendix,* Fig. S7E, H** and **Table S1**). In the TetM●70S map, the G domain of TetM is fairly well ordered, with density observable for the GDPNP nucleotide as well as for most of the nucleotide binding motif containing loops (***SI Appendix,* Fig. S7H** and **Fig. S11**). The exception is the density for the switch 1 (G2 motif) and switch 2 (G3 motif) loops that are better

visible at lower thresholds (***SI Appendix,* Fig. S7H** and **Fig. S11**): The switch 1 loop contains the putative catalytic histidine (H78), the density of which fuses at lower thresholds with the backbone of the SRL near to G2661 (***SI Appendix,* Fig. S7H**). Density for the switch 2 loop of TetM suggests that the conformation of this loop is similar to that observed for EF-Tu (11), EF-G (9), EF-2 (12) (eukaryotic EF-G homologue) and LepA (13) bound to the ribosome in the presence of non-hydrolysable GTP analogues (***SI Appendix,* Fig. S11**), whereas this loop is disordered in the ribosome-bound GDP conformations of EF-Tu (10, 14), EF-2 (12) and EF-G (1, 15) structures. However, unlike in the EF-G●GDPNP●70S (9) and LepA●GDPNP●70S (13), we observe no interaction between switch 1 and domain III of TetM, even at very low thresholds.

SI Materials and methods

Preparation of the TetM●70S complex. *Enterococcus faecalis* TetM from transposon TnFO1 (Q47810) was purified using the N-terminally encoded 6x histidine tag and Ni-NTA chromatography as described previously (8). The TetM●70S complex was formed mixing *E. coli* 70S ribosomes (0.4 μM) with tigecycline (10 μM) and then incubating at 37°C for 20 min with recombinant TetM (4 μM) in the presence of 500 μM GDPNP (Roche) in a buffer containing 20mM Hepes-KOH pH 7.8, 30 mM NH_4Cl and 10 mM $MgCl_2$. Binding of TetM to the ribosome was verified using pelleting assays, as described previously for EF-G (16).

Cryo-electron microscopy and image processing. Freshly prepared TetM●70S sample was applied to 2 nm pre-coated Quantifoil R3/3 holey carbon supported grids and vitrified using a Vitrobot Mark IV (FEI Company) and visualized on a Titan Krios TEM (FEI Company) under low-dose conditions (about 20 e− per $Å^2$) at a nominal magnification of 75,000× with a nominal defocus between −1 μm and −3.5 μm. Data was collected at 200 keV at a magnification of ×148,721 at the plane of CCD using a TemCam-F416 CMOS camera (TVIPS GmbH, 4,096 × 4,096 pixel, 15.6 μm pixel, 1 s/full frame), resulting in an image pixel size of 1.049 Å (object scale). Data collection was facilitated by the semi-automated software EM-TOOLS (TVIPS GmbH), allowing manual selection of appropriate grid meshes and holes in the holey carbon film.

Data processing was performed using the SPIDER software package (17) using an automated workflow including import of the original .tif files, automated conversion into SPIDER and MRC format, CTF determination using the SPIDER TF ED command and automated particle selection based on the program Signature (18). After initial particle selection, a second selection of the dataset was performed using MAPPOS (http://arxiv.org/abs/1112.3173v2), a newly developed machine-learning algorithm that detects wrongly selected particles ('non-ribosome particles') such as contaminations, noise, carbon edges etc. that were then omitted from the data set. Two separate datasets were collected on the same sample, with the general workflow described here for dataset 2 (similar procedure applied to dataset 1). Initially, TetM dataset 2 was comprised of 261412 particles, which were sorted into 70S ribosomes (56.2%), 50S subunits (28%) and noise-derived particles (15.8%) (***SI Appendix,* Fig. S2A**). The 70S ribosomes could be further sorted into rotated (40%) and non-rotated (33%) 70S ribosomes that lacked density for TetM as well as non-rotated 70S ribosomes with TetM bound (27%). A second data set of 145275 was collected and sorted as above. The 40776 particles from dataset 1 were combined with the 39996 particles from dataset 2, resulting in a final dataset with 52701 particles (after further refinements) with a final resolution of 7.2 Å using the Fourier shell correlation (FSC) cut-off value of 0.5 (***SI Appendix,* Fig. S2B**).

Molecular modeling and map-docking procedures. The protein homology model of *E. faecalis* TetM was generated using HHPred (19) and Modeller (20). The crystal structure of *Thermus thermophilus* EF-G●GDP trapped using the antibiotic fusidic acid in the post-translocational state (PDB2WRI) (1) served as the model template. The individual domains of the TetM homology model were then fitted as rigid bodies using Coot (21) and Chimera (22) with the clearly resolved secondary structure elements, in particularly the α-helices (***SI Appendix,* Fig. S5**), serving as constraints. In addition, density for the Switch 2 loop and GDPNP molecule, which was disordered in EF-G●GDP structure (PDB2WRI) (1), was modeled in part on the basis of the structure of *T. thermophilus* EF-Tu●GDPCP●tRNA bound to ribosome (11) (***SI Appendix,* Fig. S8**). The model was then refined in DireX (23) and manually fine-tuned using Coot (21).

The models for the 30S subunit of the TetM●70S and rotated/non-rotated 70S complexes were generated by fitting the body (1-921), head (922-1396) and helix

44/45 (1397-1530) of crystal structures (PDB and references given in the legends) as rigid bodies to the EM density using Chimera (fit in map function) (see ***SI Appendix,* Fig. S4**). The core model for the 50S subunits was generated from PDB2WWQ (24), which in turn was based on large subunit from the crystal structure of the *E. coli* 70S ribosome (25, 26). Three exceptions are that (i) H43/44 and a homology model for *E. coli* L11 generated by SWISS MODEL (27) was derived from the crystal structure of L11-RNA complex (PDB1MMS) (28) and (ii) *E. coli* L31 was based on a SWISS MODEL (27) derived a homology model using *T. thermophilus* L31 (PDB3I8I) (29) as a template (***SI Appendix,* Fig. S4**).

Mutagenesis and tetracycline resistance determination. The Quick-change mutagenesis kit (Qiagen) was used to introduce site-specific mutations into the *tetM* gene on the pET-TetM (8), according to the manufacturers instructions. The TetMΔCTE construct was generated by introducing a stop codon directly after domain V (Δ623-639). The primers for mutagenesis are listed in ***SI Appendix,* Table S2**. All mutants were confirmed by sequencing and transformed into *E. coli* BL21 strain. Overnight cultures were grown in LB at 37°C in the presence of 100μg/ml ampicillin and then diluted into fresh LB containing 1 mM IPTG and increasing concentrations of tetracycline (ranging from 0-128 μg/ml). Growth at 37°C was monitored over a period of 0-16h by measuring the optical density at 600nm with a Tecan-Infinite M1000 microplate reader. The expression of all TetM mutants was confirmed to be equivalent to that observed for the wildtype TetM using Western blotting against the 6xHis-tag.

Coordinates, alignments and figures. Alignment of all PDBs and generation of structure figures was performed using Chimera (22) and PyMol (The PyMOL Molecular Graphics System, Version 1.5.0.1 Schrödinger, LLC.). Secondary structure predictions were performed using PSIPRED (30, 31). The Cryo-EM map of the TetM●70S complex is deposited in the EMDatabank under accession number EMD-2183. The model for TetM is deposited in PDB under accession number PDB ID 3J25.

SI Text

SI References

1. Gao YG, *et al.* (2009) The structure of the ribosome with elongation factor G trapped in the posttranslocational state. *Science* **326:** 694-699.
2. Wilson DN (2009) The A-Z of bacterial translation inhibitors. *Crit Rev Biochem Mol Biol* **44:** 393-433.
3. Clementi N, *et al.* (2010) Atomic mutagenesis reveals A2660 of 23S ribosomal RNA as key to EF-G GTPase activation. *Nat Chem Biol* **6:** 344-351.
4. Datta PP, *et al.* (2005) Interaction of the G' domain of elongation factor G and the C-terminal domain of ribosomal protein L7/L12 during translocation as revealed by cryo-EM. *Mol Cell* **20:** 723-731.
5. Harms JM, *et al.* (2008) Translational regulation via L11: molecular switches on the ribosome turned on and off by thiostrepton and micrococcin. *Mol Cell* **30:** 26-38.
6. Dantley K, Dannelly H, Burdett V (1998) Binding interaction between Tet(M) and the ribosome: Requirements for binding. *J Bacteriol* **180:** 4089-4092.
7. Connell SR, *et al.* (2003) Mechanism of Tet(O)-mediated tetracycline resistance. *EMBO J* **22:** 945-953.
8. Mikolajka A, *et al.* (2011) Differential effects of thiopeptide and orthosomycin antibiotics on translational GTPases. *Chem Biol* **18:** 589-600.
9. Connell SR, *et al.* (2007) Structural basis for interaction of the ribosome with the switch regions of GTP-bound elongation factors. *Mol Cell* **25:** 751-764.
10. Schmeing TM, *et al.* (2009) The crystal structure of the ribosome bound to EF-Tu and aminoacyl-tRNA. *Science* **326:** 688-694.
11. Voorhees RM, Schmeing TM, Kelley AC, Ramakrishnan V (2010) The mechanism for activation of GTP hydrolysis on the ribosome. *Science* **330:** 835-838.
12. Taylor DJ, *et al.* (2007) Structures of modified eEF2 80S ribosome complexes reveal the role of GTP hydrolysis in translocation. *Embo J* **26:** 2421-2431.
13. Connell SR, *et al.* (2008) A new tRNA intermediate revealed on the ribosome during EF4-mediated back-translocation. *Nat Struct Mol Biol* **15:** 910-915.
14. Schuette JC, *et al.* (2009) GTPase activation of elongation factor EF-Tu by the ribosome during decoding. *Embo J* **28:** 755-765.
15. Ratje AH, *et al.* (2010) Head swivel on the ribosome facilitates translocation by means of intra-subunit tRNA hybrid sites. *Nature* **468:** 713-716.
16. Sharma MR, *et al.* (2010) PSRP1 is not a ribosomal protein, but a ribosome-binding factor that is recycled by the ribosome-recycling factor (RRF) and elongation factor G (EF-G). *J Biol Chem* **285:** 4006-4014.
17. Frank J, *et al.* (1996) SPIDER and WEB: processing and visualization of images in 3D electron microscopy and related fields. *J Struct Biol* **116:** 190-199.
18. Chen JZ, Grigorieff N (2007) SIGNATURE: a single-particle selection system for molecular electron microscopy. *J Struct Biol* **157:** 168-173.
19. Soding J, Biegert A, Lupas AN (2005) The HHpred interactive server for protein homology detection and structure prediction. *Nucleic Acids Res* **33:** W244-248.
20. Eswar N, *et al.* (2008) Protein structure modeling with MODELLER. *Methods Mol Biol* **426:** 145-159.

21. Emsley P, Cowtan K (2004) Coot: Model-Building Tools for Molecular Graphics. *Acta Crystallographica Section D - Biological Crystallography* **60:** 2126-2132.
22. Pettersen EF*, et al.* (2004) UCSF Chimera - A Visualization System for Exploratory Research and Analysis. *J Comput Chem* **25:** 1605-1612.
23. Schroder GF, Brunger AT, Levitt M (2007) Combining efficient conformational sampling with a deformable elastic network model facilitates structure refinement at low resolution. *Structure* **15:** 1630-1641.
24. Seidelt B*, et al.* (2009) Structural insight into nascent polypeptide chain-mediated translational stalling. *Science* **326:** 1412-1415.
25. Schuwirth B*, et al.* (2005) Structures of the bacterial ribosome at 3.5 Å resolution. *Science* **310:** 827-834.
26. Berk V, Zhang W, Pai RD, Cate JH (2006) Structural basis for mRNA and tRNA positioning on the ribosome. *Proc Natl Acad Sci U S A* **103:** 15830-15834.
27. Kiefer F*, et al.* (2009) The SWISS-MODEL Repository and associated resources. *Nucleic Acids Res* **37:** D387-392.
28. Wimberly BT*, et al.* (1999) A detailed view of a ribosomal active site: The structure of the L11-RNA complex. *Cell* **97:** 491-502.
29. Jenner L, Demeshkina N, Yusupova G, Yusupov M (2011) Structural rearrangements of the ribosome at the tRNA proofreading step. *Nat Struct Mol Biol* **17:** 1072-1078.
30. Jones DT (1999) Protein secondary structure prediction based on position-specific scoring matrices. *J Mol Biol* **292:** 195-202.
31. Buchan DW*, et al.* (2010) Protein annotation and modelling servers at University College London. *Nucleic Acids Res* **38:** W563-568.
32. Leijonmarck M, Liljas A (1987) Structure of the C-terminal domain of the ribosomal protein L7/L12 from *Escherichia coli* at 1.7 Å. *J Mol Biol* **195:** 555-580.
33. Bhushan S*, et al.* (2011) SecM-stalled ribosomes adopt an altered geometry at the peptidyltransferase center. *PLoS Biol* **19:** e1000581.
34. Brodersen DE*, et al.* (2000) The structural basis for the action of the antibiotics tetracycline, pactamycin, and hygromycin B on the 30S ribosomal subunit. *Cell* **103:** 1143-1154.
35. Pioletti M*, et al.* (2001) Crystal structures of complexes of the small ribosomal subunit with tetracycline, edeine and IF3. *EMBO J* **20:** 1829-1839.

SI Figures

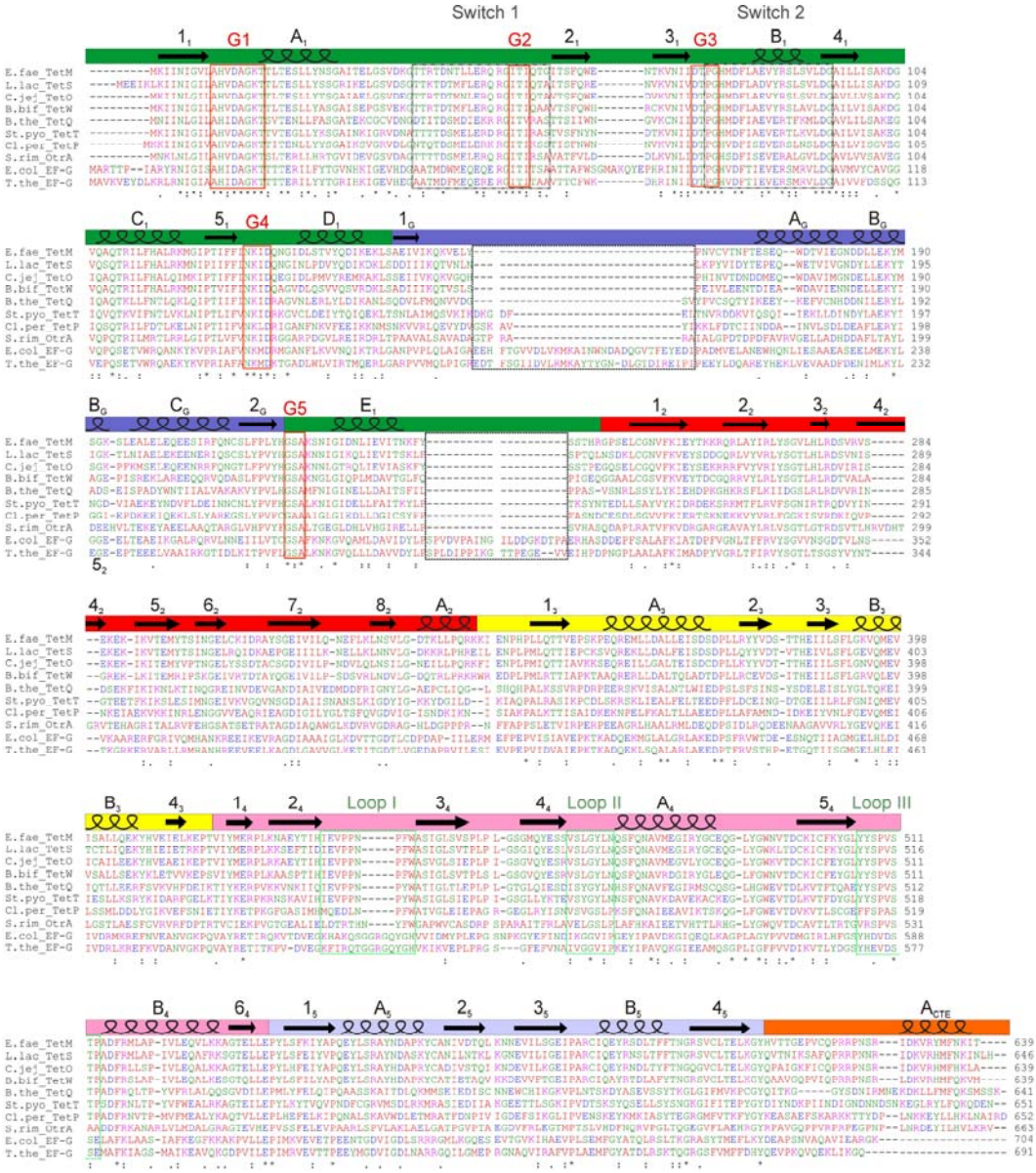

Figure S1 Alignment of RPP sequences and EF-G. ClustalW2 alignment of RPP sequences from *Enterococcus faecalis* (E.fae_TetM), *Lactococcus lactis subsp. lactis* (L.lac_TetS), *Campylobacter jejuni* (C.jej_TetO), *Bifidobacterium bifidum* (B.bif_TetW), *Bacteroides thetaiotaomicron* (B.the TetQ), *Streptococcus pyogenes* (St.pyo_TetT), *Clostridium perfringens* (Cl.per_TetP), *Streptomyces rimosus* (S.rim_OtrA) and *Escherichia coli* and *Thermus thermophilus* EF-G (E.col EF_G and T.the_EF-G). Domain boundaries are shown for domains I (G domain, green and G' subdomain, blue), II (red), III (yellow), IV (pink), V (pale blue) and C-terminal extension (CTE, orange) with secondary structure assignments and nomenclature for the *E. faecalis* TetM homology model. The G1-G5 nucleotide binding motifs, switch 1 and 2 loops as well as the TetM domain IV loops I-III are also indicated.

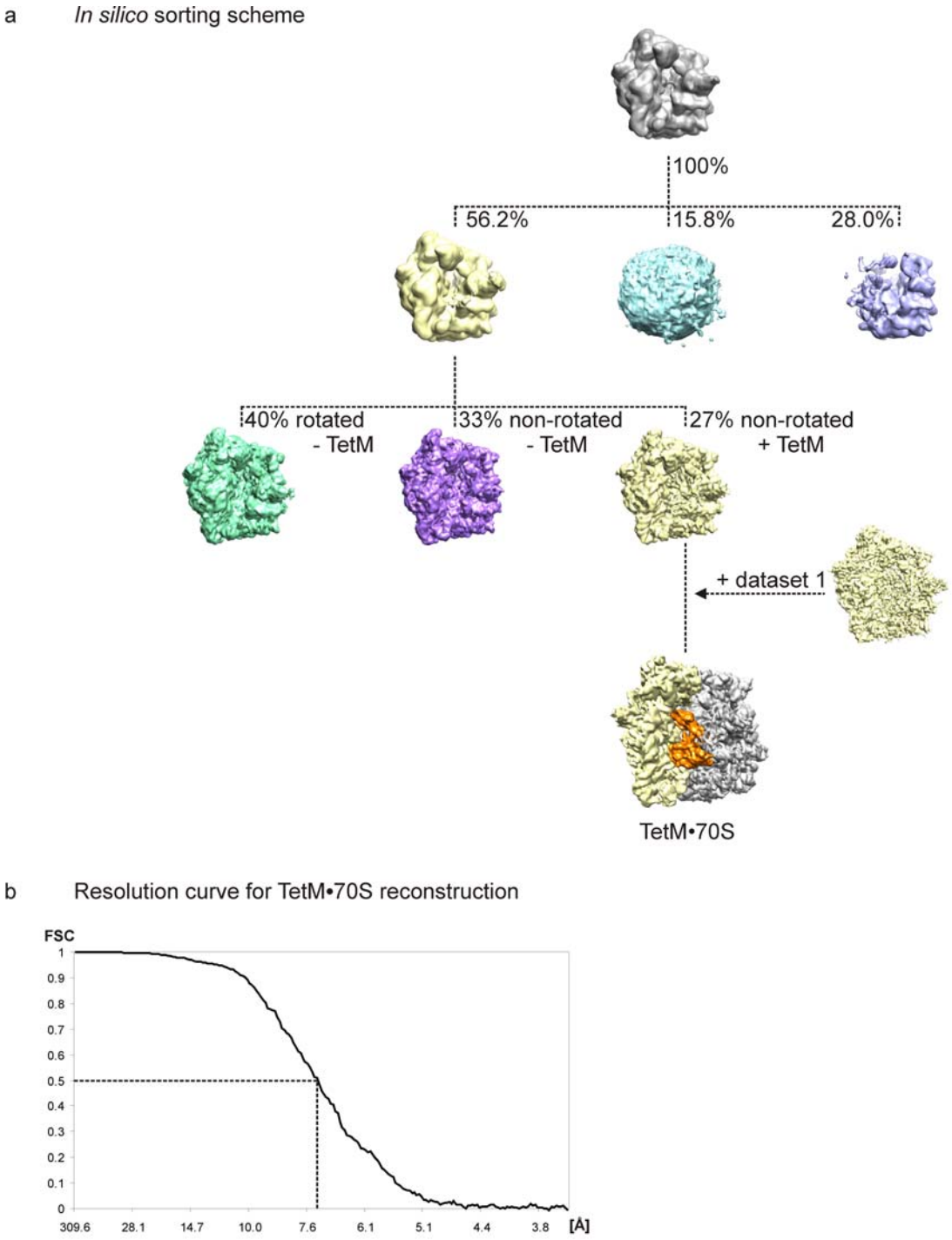

Figure S2 *In silico* sorting and resolution of the TetM●70S complex. (**A**) The dataset was sorted into sub-datasets containing healthy ribosomal particles, noisy/edged particles and 50S subunits. Subsequently, ribosome particles were sorted into non-rotated and rotated ribosomes without TetM and TetM-bound ribosomes. TetM●70S particles from dataset 1 were then joined with this dataset and after improvement, a final map could be visualized showing TetM (highlighted in orange) bound to the ribosome with (**B**) a resolution of 7.2 Å using the Fourier shell correlation (FSC) cut-off value of 0.5.

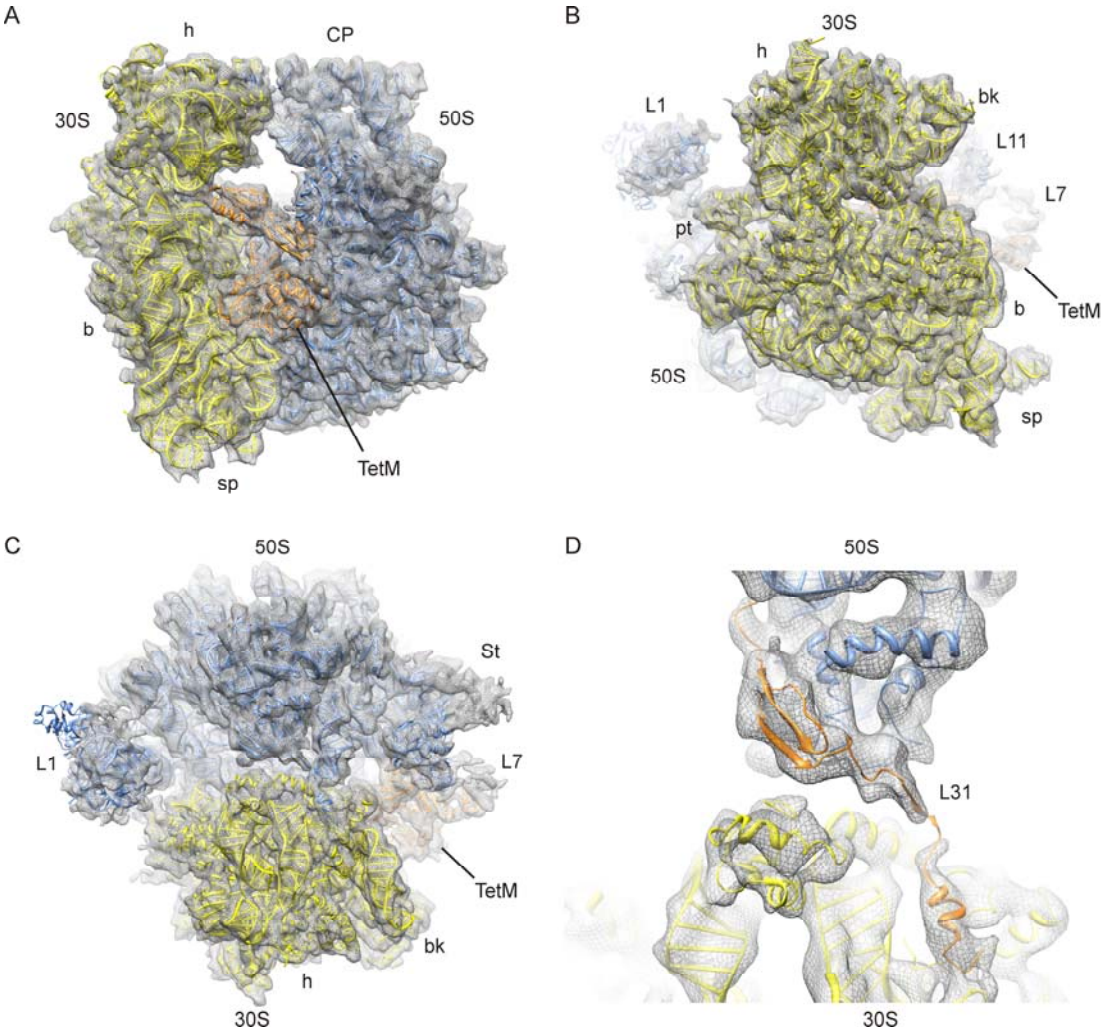

Figure S3 Electron density and fit of a molecular model for the TetM•70S complex. (**A-C**) Cryo-EM density (grey mesh) with fitted molecular model for the *E. coli* 30S (yellow, PDB2AVY)(25, 26) and 50S (blue, PDB2WWQ(24)/1MMS(28)/1CTF(32)) subunit, as well as TetM (orange), viewed from (**A**) factor binding site, (**B**) 30S solvent side and (**C**) birds-eye view onto top of ribosome. (**D**) Molecular model for *E. coli* ribosomal protein L31 (orange) based on the *T. thermophilus* L31 from PDB3I8I(29) fitted into the remaining cryo-EM density after fitting of the crystal structures of the *E. coli* 30S and 50S subunits.

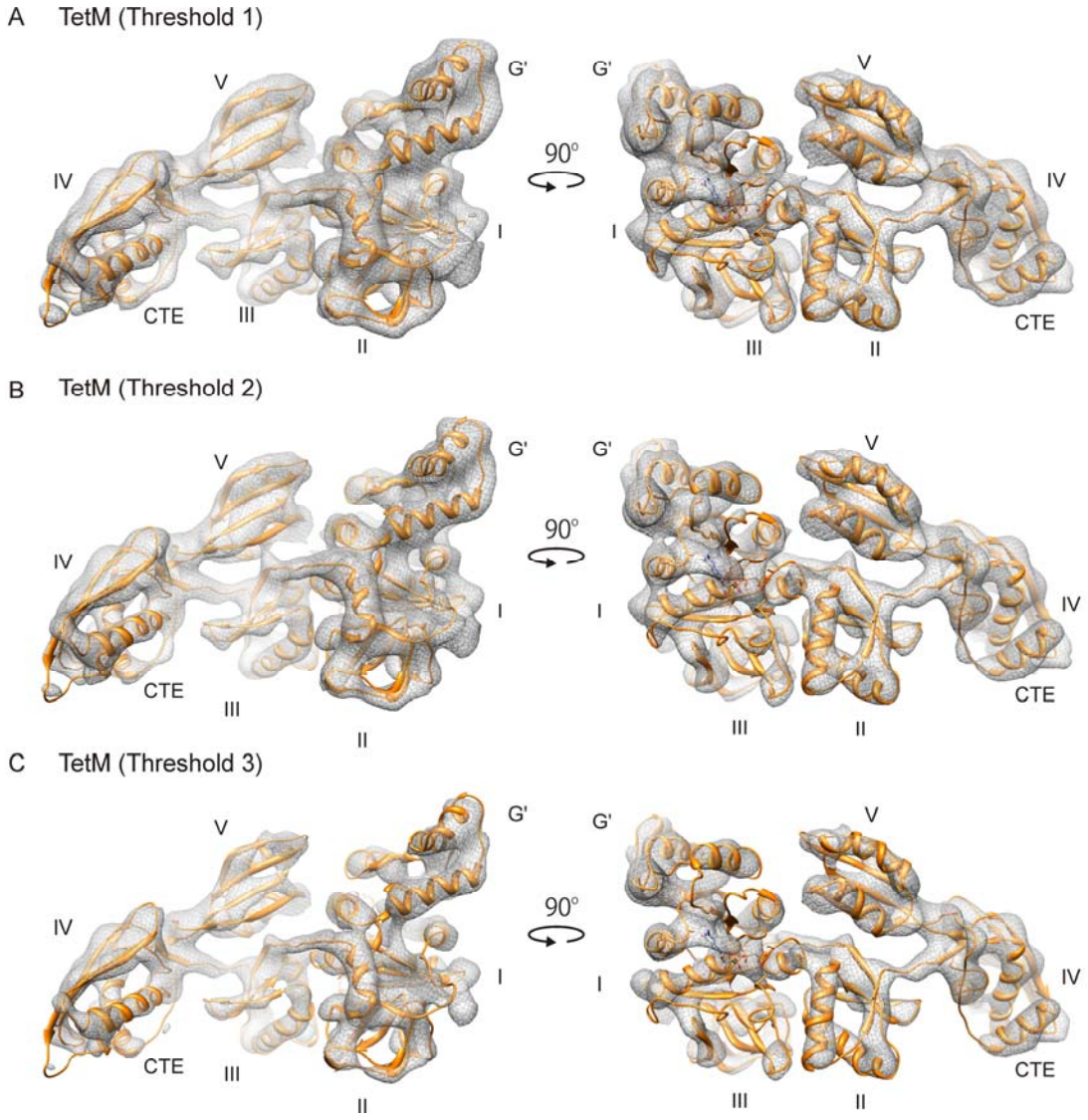

Figure S4 Electron density and model for TetM at different thresholds. (**A-C**) Two views of the isolated cryo-EM density for TetM from the TetM●70S complex, shown at increasing thresholds ranging from (**A**) 2 σ, (**B**) 3 σ to (**C**) 4 σ. The domains are labeled I-V as well as the G' subdomain and C-terminal extension (CTE). Note the persistence of cylindrical rods for α-helices at higher thresholds (**C**), such as the terminal helix in the CTE.

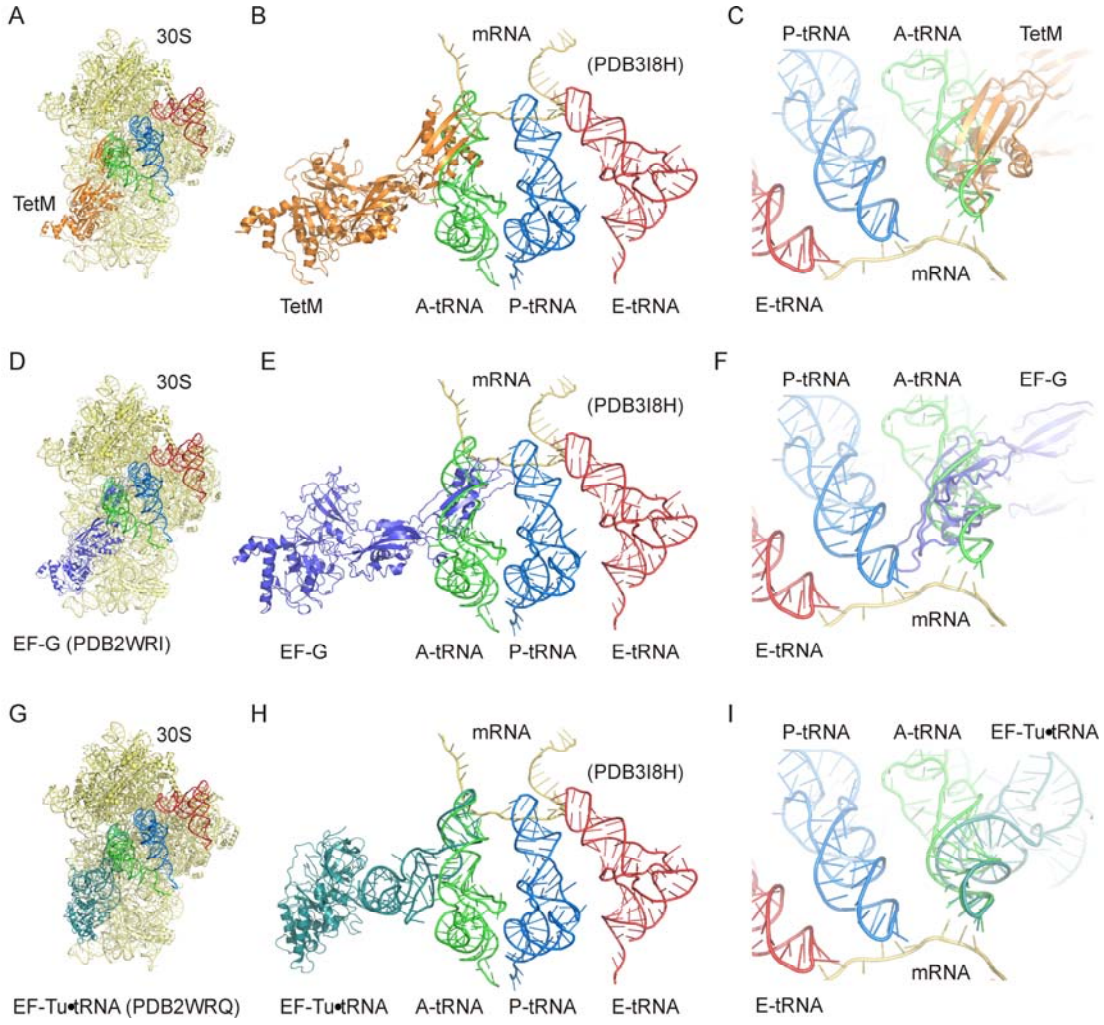

Figure S5 Relative position of TetM, EF-G and EF-Tu compared to tRNA and mRNA. (**A-I**) Relative binding position of (**A-C**) TetM, (**D-F**) EF-G (PDB2WRI)(1) and (**G-I**) EF-Tu●tRNA (PDB2WRQ)(10) on the 30S subunit (yellow) compared to messenger RNA (mRNA, tan) and A- (green), P- (blue) and E-site (red) tRNAs (taken from PDB3I8H)(29). Note that TetM overlaps significantly with the position of the A-tRNA but does not approach the P-tRNA.

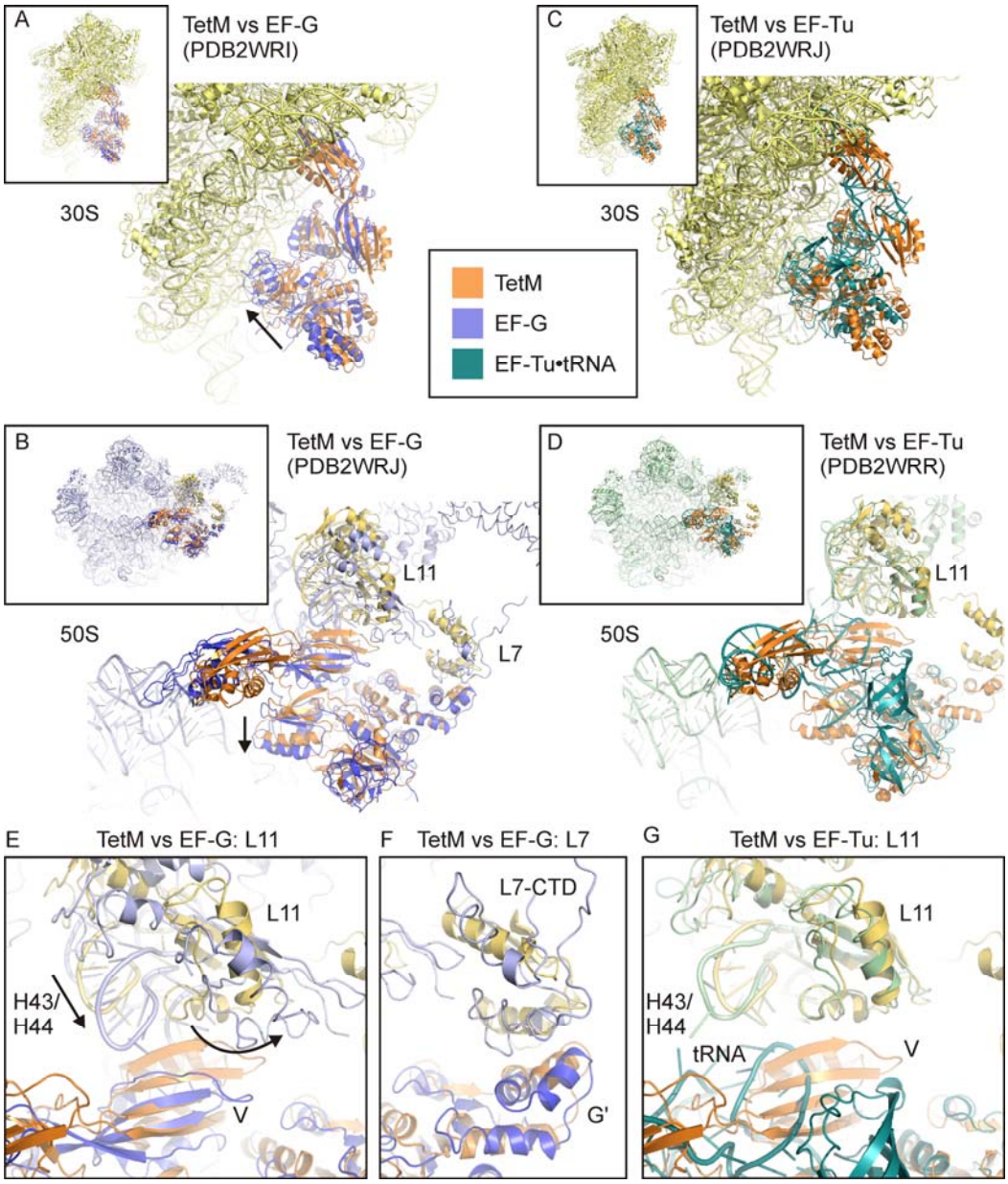

Figure S6 Comparison of TetM on the ribosome relative to EF-G and EF-Tu. (**A-G**) Comparison of ribosome binding positions and interactions of TetM (orange) with (**A,B,E,F**) EF-G (blue, PDB2WRI)(1) and (**C,D,G**) EF-Tu●tRNA (PDB2WRQ)(10), aligned relative to the (**A,C**) 16S rRNA of the 30S subunit (yellow) and (**B,D-G**) 23S rRNA of the 50S subunit. In (**B,D-G**), the stalk base (H43-H44 and L11) and C-terminal domain (CTD) of L7 of the 50S subunit when TetM bound is shown in yellow. Arrows in (**A,B**) indicate the shift in EF-G (relative to TetM) closer to the 30S subunit and away from the 50S subunit. Arrows in (**E**) indicate the shifted position of the stalk base and NTD of L11 in the EF-G●70S (blue) compared to the TetM●70S (yellow) complex, whereas the respective conformations for EF-Tu are similar to that observed for TetM (**G**).

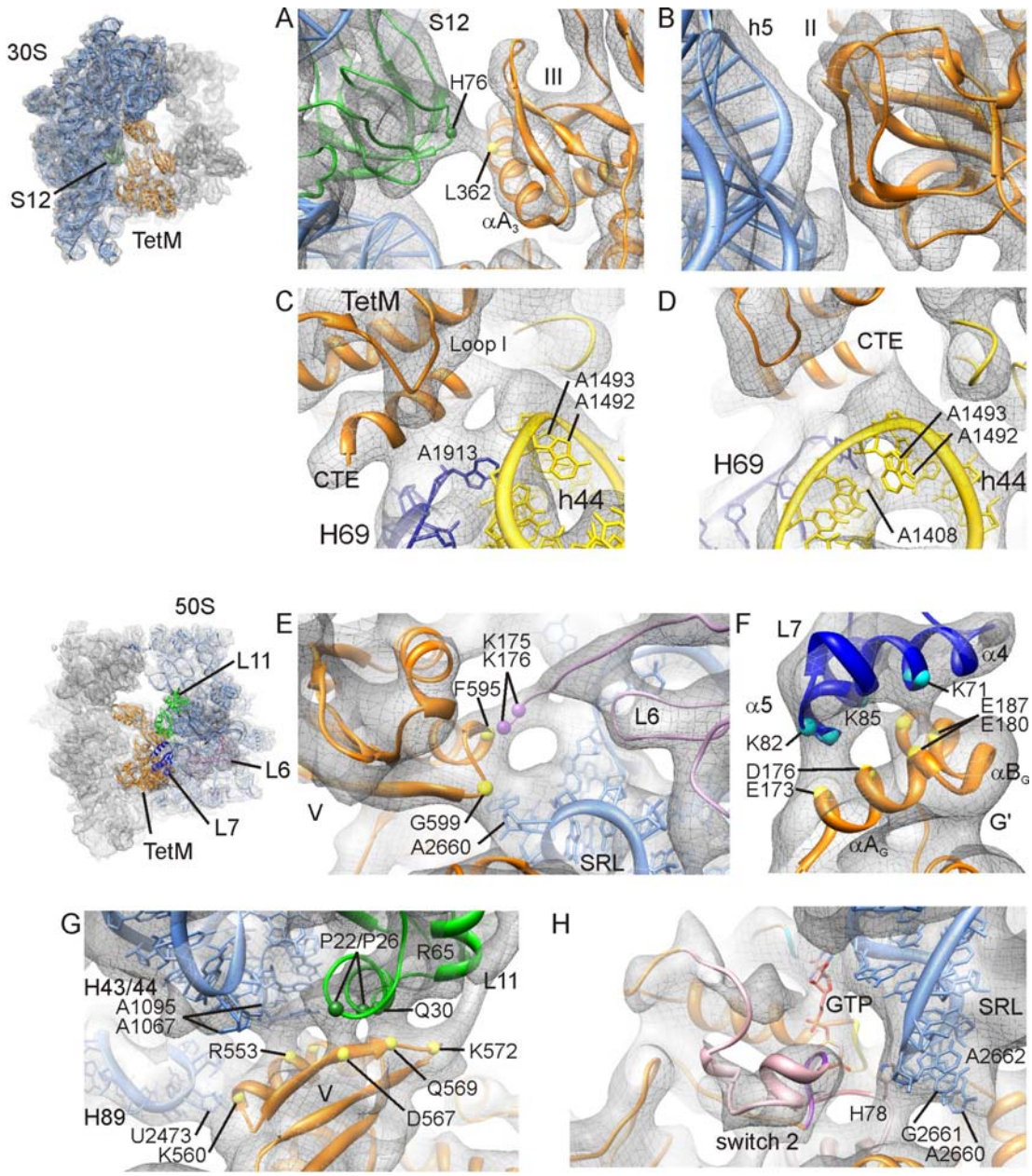

Fig. S7 Interaction of TetM with the 70S ribosome. Predicted contact sites (spheres in model taken from **Table S1**) between density (grey mesh) of TetM and the (**A-D**) 30S and (**E-H**) 50S subunit. (**A**) Helix αA_3 of domain III of TetM (orange) interacts with S12 (green), whereas (**B**) no interaction is observed between TetM-domain II (orange) and 16S rRNA helix 5 (h5, blue). (**C,D**) The CTE of TetM interacts with h44 (the flipped-in conformation of A1492/3 is shown). Large subunit contacts with TetM include (**E**) domain V of TetM (orange) with A2660 of the SRL (H95) (blue) and the CTE of L6 (purple), (**G**) domain V of TetM (orange) with H89, the tips of H43 and H44 as well as with L11 (green), (**F**) helices αA_G and αB_G of the G' subdomain of TetM (orange) with the C-terminal domain of L7/L12 (blue), and (**H**) interaction between domain I (G domain) of TetM (orange with switch 2 loop in pink/purple) and the SRL (blue).

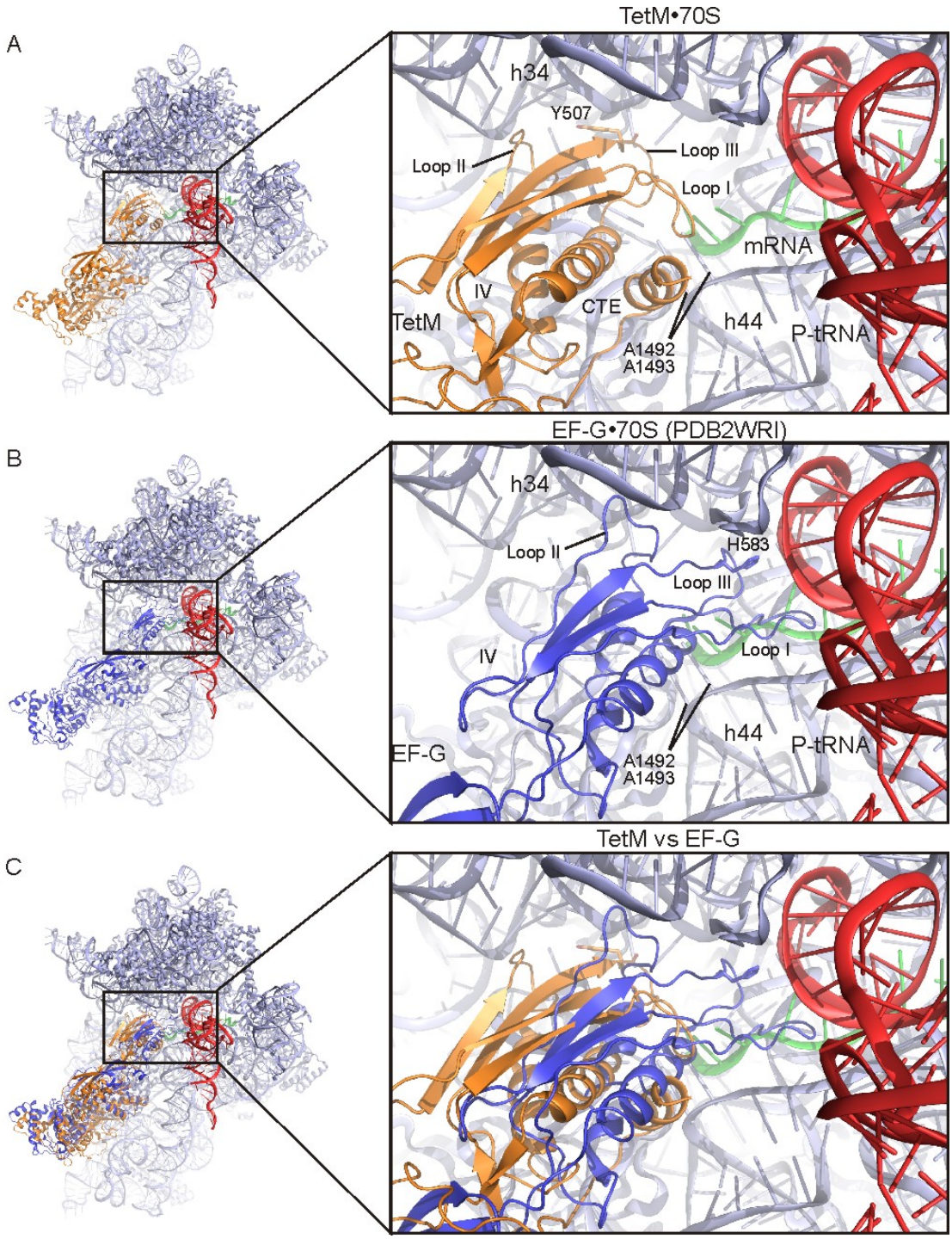

Figure S8 Comparison of the orientation of domain IV of TetM and EF-G on the ribosome. (**A-B**) Comparison of the binding position of (**A**) TetM (orange) and (**B**) EF-G (PDB2WRI)(1) relative to mRNA (green) and P-tRNA (red) (taken from PDB3I8H)(29), with zoom showing domain IV of (**A**) TetM and (**B**) EF-G and the respective orientations of Loops I-III. Histidine 583 (H583) in Loop III of EF-G and the equivalent tyrosine (Y507) in Loop III of TetM are shown as sticks. (**C**) Superimposition of (**A**) and (**B**).

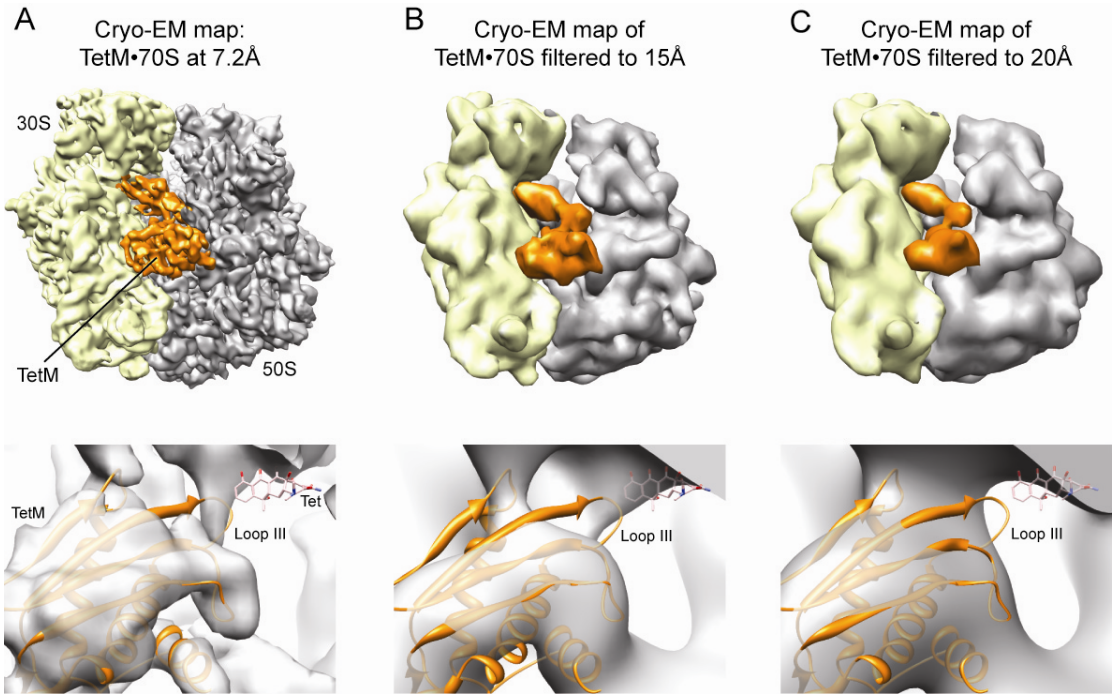

Figure S9 Filtering of the TetM●70S complex to lower resolutions. (**A**) Electron density map of the TetM●70S complex at 7.2 Å compared with the same map filtered at (**B**) 15 Å and (**C**) 20 Å. The upper panel shows an overview with TetM (orange), 30S (yellow) and 50S (grey), while the lower panel shows zoomed view focused on domain IV of TetM with PDB model (orange) and map (grey surface), compared with the binding position of tetracycline (Tet). Note the loss of density for loop III of domain IV of TetM at lower resolutions.

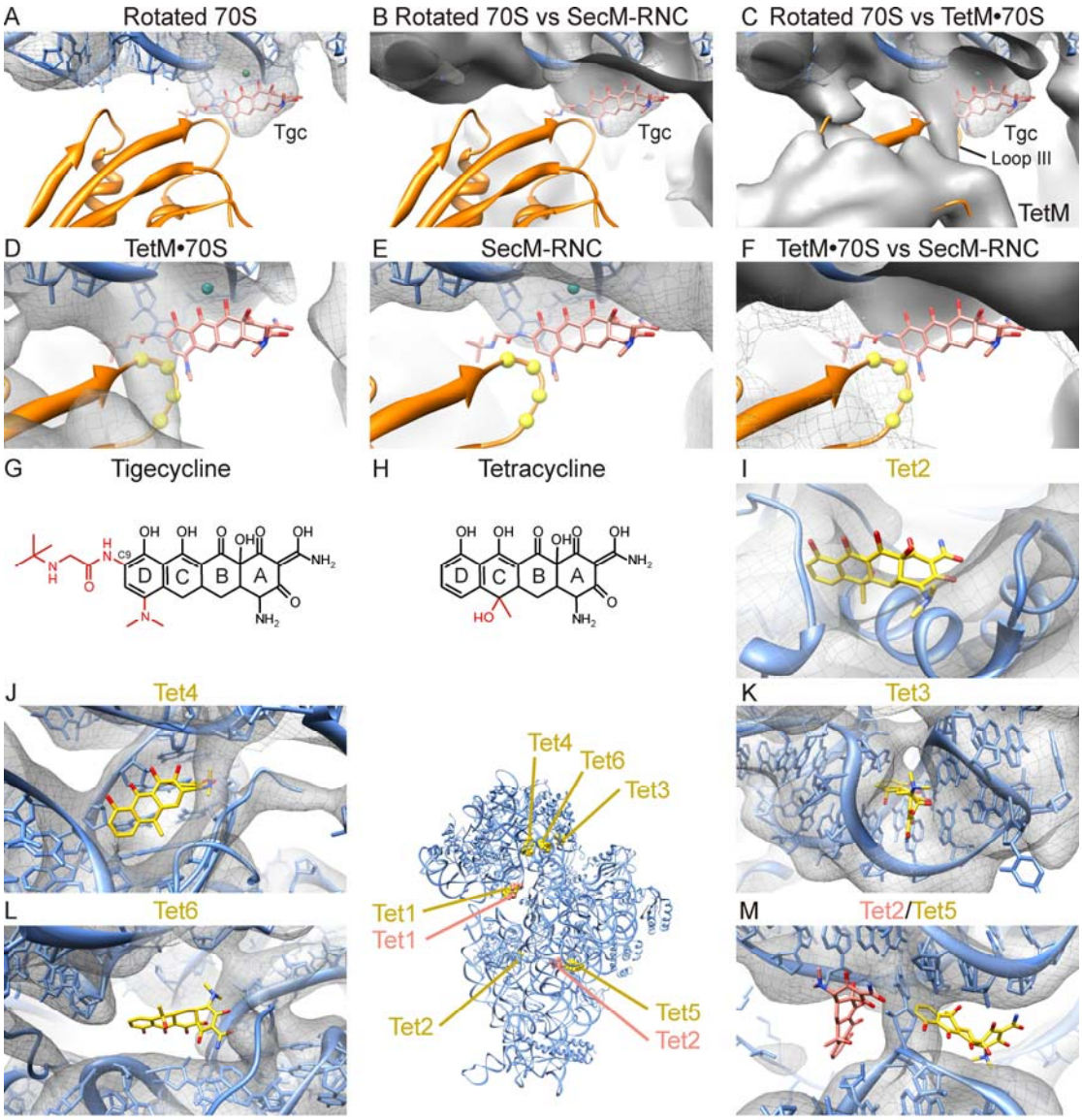

Figure S10 Binding sites of tigecycline and tetracycline on the ribosome. (**A-C**) Electron density map (grey mesh) of the (**A**) rotated 70S map without TetM from sorting (**Fig. S2**) that reveals density for tigecycline, compared with (**B**) SecM-RNC (EMD-1829)(33) and (**C**) TetM●70S. In (**B,C**), the rotated 70S map is shown as a grey mesh and the SecM-RNC and TetM maps as opaque grey surfaces. (**G,H**) Chemical structures for tigecycline and tetracycline, with differences highlighted in red. (**I-M**) Overview of tetracycline binding sites of the 30S subunit(34, 35) with enlargements showing lack of density in the TetM●70S map (grey mesh) for secondary binding sites, Tet1 and Tet2 (red)(34) and Tet1-Tet6 (gold)(35).

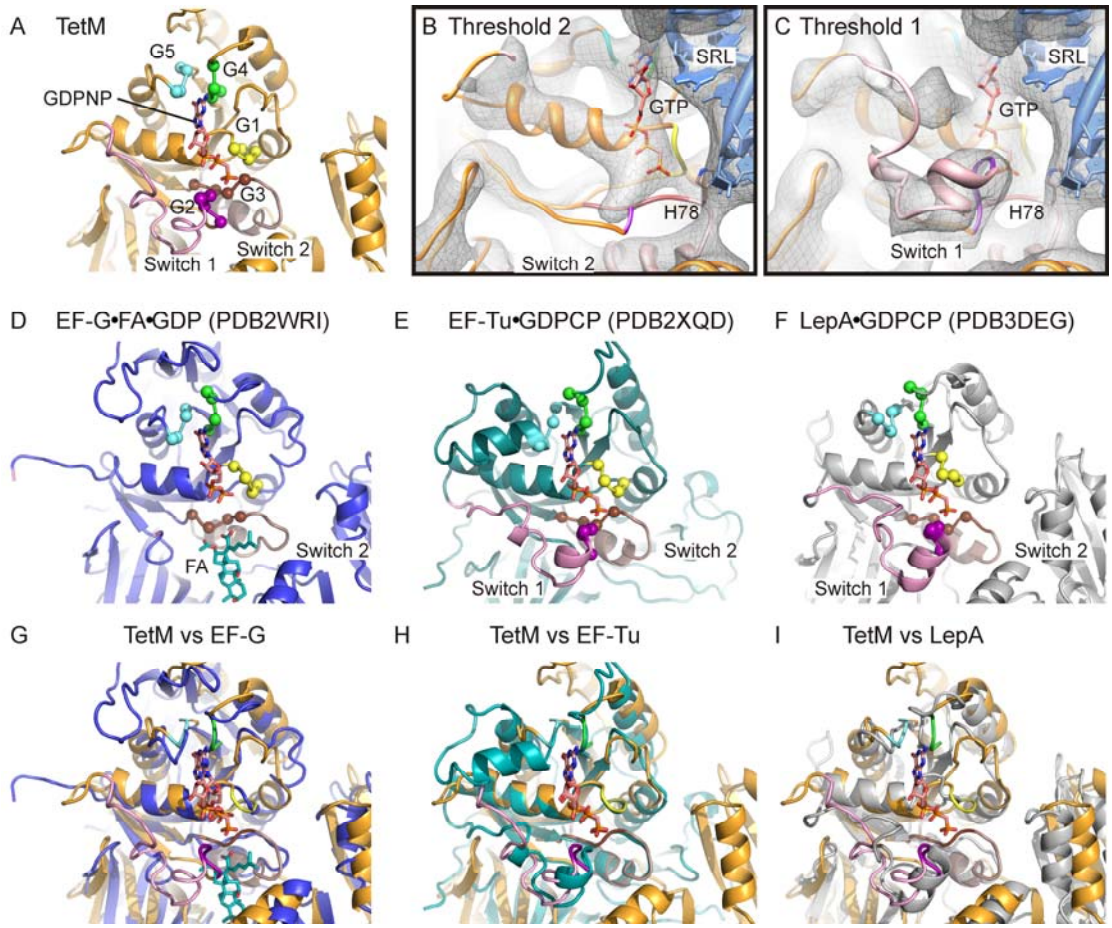

Figure S11 Comparison of G domains of TetM, EFG, EF-Tu and LepA. (**A**) Ribbon representation of the G domain of TetM (orange) with nucleotide binding motifs G1 (yellow), G2 (purple), G3 (brown), G4 (green), G5 (cyan) and switch 1 (pink) and switch 2 (light brown) highlighted. (**B,C**) Electron density of the G domain of TetM shown at (**B**) high and (**C**) low thresholds. Note that at low threshold additional density appears that would correspond with the conformation of the switch 1 as observed previously for EF-Tu●tRNA trapped on the ribosome with GDPCP (PDB2XQD)(11). Note that lack of density for part of the switch 2 in the region of the catalytic histidine 78 (H78). (**D-F**) Ribbon representation of the G domain with same view as (**A**) but for (**D**) EF-G●FA●GDP●70S complex (blue, PDB2WRI) with disordered switch 1, (**E**) EF-Tu●tRNA●GDPCP●70S complex (teal, PDB2XQD)(11) and (**F**) LepA●GDPCP●70S complex (grey, PDB3DEG). (**G-I**) Superimposition of (**A**) with (**D**)-(**F**). Note the similarity in the conformation of the switch 1 region of TetM with (**H**) EF-Tu and (**I**) LepA.

SI Tables

Table S1 Contacts between TetM and the ribosome

TetM			Ribosome*		σ
Domain	**Region**	**Residue**	**Region**	**Residue**	
G	GTP	Guanine	23S rRNA, H95 (SRL)	G2655	4.0
	loop between 3_1 and B_1	H78, M79	23S rRNA, H95 (SRL)	G2661	3.9
	loop between 4_1 and C_1	K102	23S rRNA, H95 (SRL)	A2657	2.6
	C1	Q106, A107	23S rRNA, H95 (SRL)	A2660	2.5
	loop between 5_1 and D_1	Q132, N133	23S rRNA, H95 (SRL)	U2656, A2657	2.1
	loop between 5_1 and D_1	G134	L6	V91, G92	2.7
	loop between E_1 and 1_2	Y161	L6	Q127	1.4
G'	A_G	E173, D176	L7-CTD, helix α5	G80-K82	3.6
	B_G	E180, E187	L7-CTD, helix α4	K71	2.1
	B_G	S191	L7-CTD, helix α4	K85	2.3
III	A_3	L362	S12	H76	4.6
IV	**loop II** between 4_4 and A_4	S465, L466, G467	16S rRNA, h34 (head)	backbone C1208, C1209	3.7
	loop III between 5_4 and B_4	Y507, S508, P509	16S rRNA, h34 (head)	backbone U1052 G1053, C1054	2.3
	loop III between 5_4 and B_4	P513	16S rRNA, h18 (body)	C518	3.9
V	A5	R553, N556	23S rRNA, H43/H44	A1067, A1095	2.5
	A5	K560	23S rRNA, H89	U2473	5.0
	2_5	D567, Q569	L11 3_{10}-helix	P22, P26 Q30	3.1
	loop between 2_5 and 3_5	K572	L11 3_{10}-helix	R65	2.8
	B5	F595, F596	L6	K175, K176	4.0
	B5	N598-R600	23S rRNA, H95 (SRL)	A2660	6.4
CTE	loop between 4_5 and C_5	R627	16S rRNA, h44	A1492, A1493	2.5
	A_{CTE}	I628	16S rRNA, h44	A1492, A1493	2.5
	A_{CTE}	Y633, M634 F635	23S rRNA, H69	A1913, C1914	6.3

* shaded yellow = 30S components and shaded blue = 50S components

Table S2 Primers for site-directed mutagenesis

Construct	Primer sense/ antisense (5' – 3')
TetM-Y506A	5'-GTTTTAAGTATGGCTTAGCGTATAGCCCTGTTAGTAC-3' 5'-GTACTAACAGGGCTATACGCTAAGCCATACTTAAAAC-3'
TetM-Y507A	5'-AAGTATGGCTTATACGCGAGCCCTGTTAGTACC-3' 5'-GGTACTAACAGGGCTCGCGTATAAGCCATACTT-3'
TetM-S508A	5'-GTATGGCTTATACTATGCGCCTGTTAGTACCCCAGC-3' 5'-GCTGGGGTACTAACAGGCGCATAGTATAAGCCATAC-3'
TetM-P509A	5'-GTATGGCTTATACTATAGCGCGGTTAGTACCCCAGCAG-3' 5'-CTGCTGGGGTACTAACCGCGCTATAGTATAAGCCATAC-3'
TetM-V510A	5'-CTTATACTATAGCCCTGCGAGTACCCCAGCAGATTTTC-3' 5'-GAAAATCTGCTGGGGTACTCGCAGGGCTATAGTATAAG-3'
TetM-S511A	5'-CTTATACTATAGCCCTGTTGCGACCCCAGCAGATTTTC-3' 5'-GAAAATCTGCTGGGGTCGCAACAGGGCTATAGTATAAG-3'
TetM-YY/AA	5'-GTTTTAAGTATGGCTTAGCGGCCAGCCCTGTTAGTACC-3' 5'-GGTACTAACAGGGCTGGCCGCTAAGCCATACTTAAAAC-3'
TetM-YSP/AAA	5'-AAGTATGGCTTATACGCGGCCGCGGTTAGTACCCCAGCA-3' 5'-TGCTGGGGTACTAACCGCGGCCGCGTATAAGCCATACTT-3'
TetM-SPV/AAA	5'-GTATGGCTTATACTATGCGGCCGCGAGTACCCCAGCAGAT TTTCGG-3' 5'-CCGAAAATCTGCTGGGGTACTCGCGGCCGCATAGTATAAG CCATAC-3'
TetMΔCTE (ΔR_{623}-T_{639})	5'-GTTTGCCAGCCCCGTTAACCGGGCTTCTCCTCAAATCTC-3' 5'-GAGATTTGAGGAGAAGCCCGGTTAACGGGGCTGGCAAAC-3'